Chapter-2

Synthesis and Characterisation of Amino acid-capped transition metal ion-doped iron oxide nanoparticles

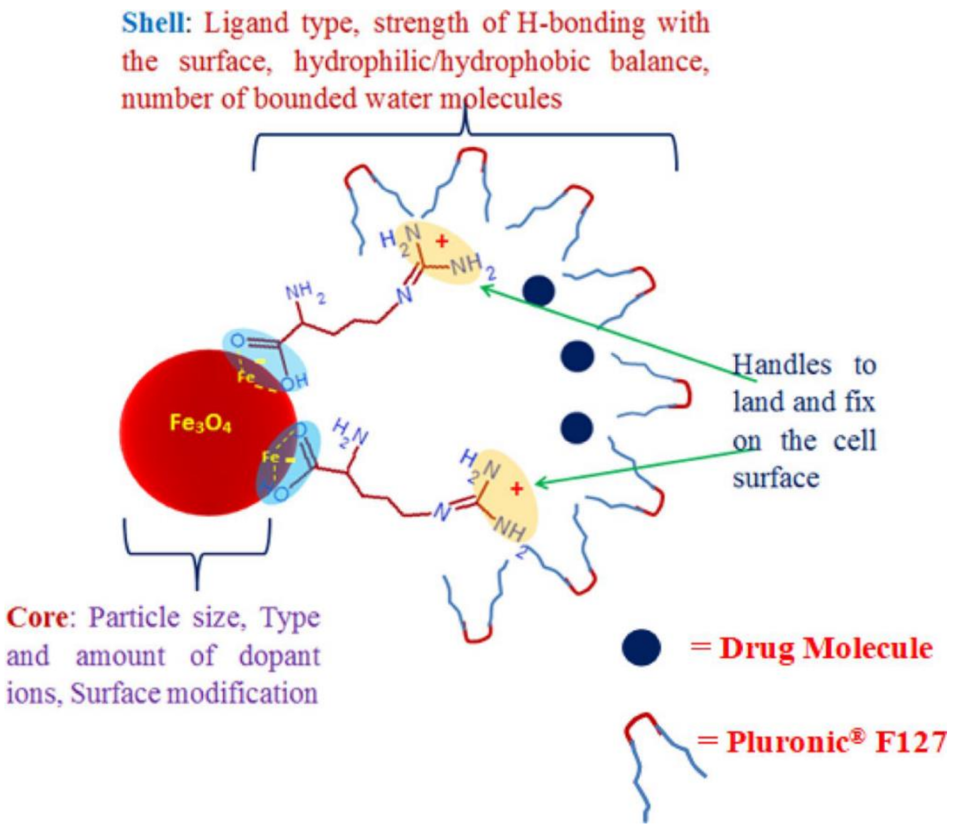

2.1 Introduction

Materials chemistry with the introduction of nanotechnology has carried about numerous nanomaterials and multi-functional materials which is come from with interesting properties into the scientific world. Even a small perform of a nanomaterial carries about huge changes in its activity and selectivity that could be positively use in many applications such as biological applications, as one of the major and important needs at current time is for point-of-care devices that can deliver perfect, reliable, and reproducible results for the detection of various physiological situations.

In this direction, an important group of metal oxide such as iron oxide nanoparticles have been synthesized, characterized, and studied for their essential properties in various fields. Among all transition metals, iron has been the essential transition element which is broadly used for studied and engineered in material chemistry. Iron can be change into useful materials which is use in daily life with expected properties and these features has engrossed researcher around the world to explore the major properties of iron.

Iron oxides, one of the important moiety of iron are preferred and use for the preparation of multi-functional magnetic nanomaterials and find unique applications in modern science, particularly in the areas like drug delivery, cellular imaging, hyperthermia induction, bio sensing, and protein separation, contrasting agents in MRI [1], magnetic storage device [2] and solar cells by photo-assisted electrolysis of water [3] Figure 2.1. Many phases of iron oxides are reported like Magnetite, HematiteGoethite, Akaganeite, Feroxyhyte, Bernalite, Iron (II) hydroxide, Ferrihydrite, Wüstite. These phases are characterized by their trivalent state, different colors, and low solubility [4]. The properties of iron oxide nanoparticles are highly depended on their synthesis procedure which is produced challenge to synthesis these nanoparticles successfully due to the particle size, oxidation state, stoichiometry or the magnetic property [5]. The advantage of using magnetite for these applications are non-toxic and decomposes into iron acting as an iron pool required for the synthesis of hemoglobin during erythropoiesis.

Magnetism is one of the basic forces that exist in the universe. It is also responsible for burgeoning evolution of life in its present form on earth. Throughout the long period of evolution, nature learns how to exploit magnetism for sophisticated biological processes. Nature exploits magnetism in all its aspects for different biochemical processes in various species. For this purpose, magnetic material based on iron oxide is preferred. For example, magnetotactic bacteria (MTB) can orient themselves according to the position of the north pole of earth, aid them to move their position towards the optimal concentration of oxygen in ocean. They can do this job by producing magnetite crystals (Fe_3O_4) in their organelles called magnetosomes [6]. It can also aid the pigeons and other migratory birds travel in proper direction.

This is made possible due to the small spot on the beak of these birds and specialized cells in their eyes rendering them capable of sensing the magnetic field [7]. Juvenile pacific salmon use these tiny magnetite crystals in their tissues to help them make their way from far out in the ocean back to their inland spawning locations [8-9]. These properties of magnetite can be used in modern science, particularly in medicinal science in the areas like drug delivery, imaging cellular processes at the molecular level or as a contrast agent (CAs) for MRI, for induction of hyperthermia, bio sensing and protein separation [10 -17].

The advantages of using magnetite for these applications are: it is non-toxic and decomposes into iron acts as an iron pool required for the synthesis of hemoglobin during erythropoiesis [18]. However, in bulk form, magnetite is paramagnetic having a large number of magnetic domains oriented randomly in the absence of applied magnetic field. On the application of a magnetic field, they orient themselves in a single direction and revert to the random state on removal of the field. However, it leaves some residual magnetization (ferrimagnetic behavior) which is not desirable in applications like MRI contrast agents (CAs) or drug delivery platforms [19-20]. It was observed that on decreasing the particle size to about 20 nm, these domains merged into a single domain having one collective magnetization direction on applying the field and further, immediately got demagnetized on removal of the field (superparamagnetic behavior) [21-22]. Any material having this property is perfect enough to serve as a drug delivery vehicle. However, on decreasing the particle size, it has a natural tendency to agglomerate [23-24]. The suspension of magnetite having very less particle size in a given solvent system is unstable. To make a stable suspension and prevent agglomeration, the surface of the particle is coated with molecules of surface active agents like CTAB, SDS etc. However, such suspension shows toxicity at physiological pH. Hence, the surfactant free synthesis of Fe_3O_4 nanoparticles (NPs) is desired [25-28].

The uniform particle size (monodispersity) of the suspension is very important. It is achieved by carrying the synthesis in a non-aqueous high boiling organic solvent (dodecane, oleylamine) at high temperature in presence of coordinating solvent which requires stringent experimental control, [29] resulting in water insoluble ferro-fluid. A tedious procedure like ligand exchange through dialysis for more than 24 h is required to make the material hydrophilic and water soluble [30]. Even then, after such processes, incomplete ligand exchange results in the loss of colloidal stability in aqueous media.

In this direction, many different methods have been invented and improved to develop multi-functional iron oxide nanoparticles. Some reported methods for iron oxide nanoparticles are listed here such as hydrothermal process and electrochemical [31–37], micro-emulsions techniques [38-39], electrospray process [40], sono-chemical [41-42], microwave assisted synthesis [43-45], vapour phase approach and micro-plasma [46-47] and green synthesis [48–52] Figure 2.1.

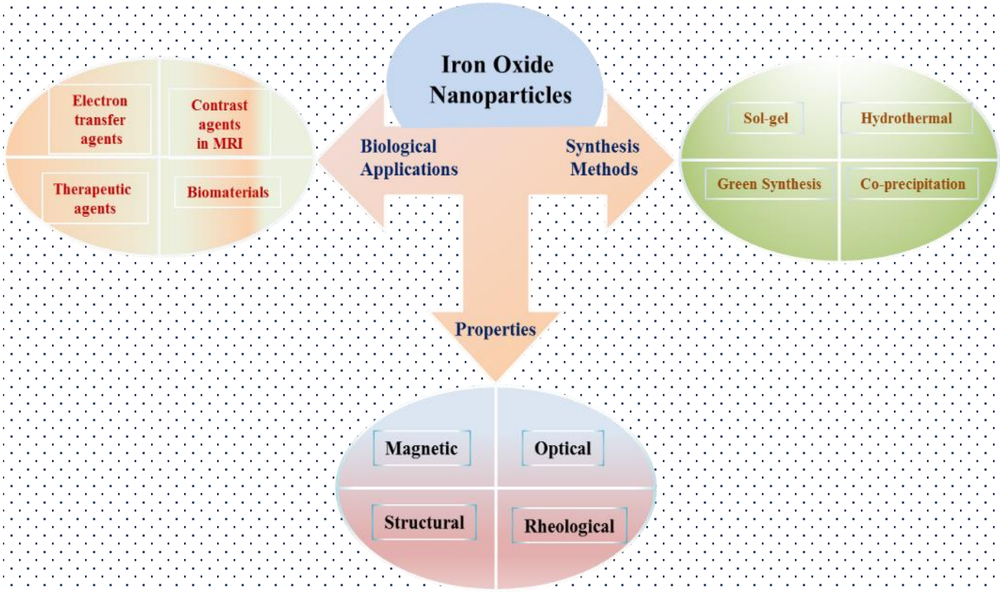

Fig. 2.1. Synthesis methods, properties and biological applications of iron oxide nanoparticles

Most of the syntheses reported to date are carried out in constrained conditions to stringently control the particle size and phase purity of the magnetite. However, during large-scale production, such conditions may not be strictly followed as some minute errors during unit operations could result in wastage of the total batch and make it economically unviable. Hence, it is important to discuss the different synthesis process by which iron oxide nanoparticles are prepared to benefit with the required properties such as surface, electrical, optical, and mainly magnetic properties for innumerable applications. In this paper, we have synthesized Ultra-Small Iron Oxide NPs (Fe_3O_4-USIONs) and ferrites (MFe_2O_4) by an easy co-precipitation method. We focused on tuning the intrinsic magnetic property of USIONs by varying the transition metal dopant ions under the same reaction conditions rather than adopting the solvothermal or any other tedious synthesis methods. A variety of amino acids, such as L-proline [53], L-histidine and L-arginine [54], guanidine [55] were reported and characterized by spectroscopic methods and used for various organic transformation but very few examples are available to prepared iron oxide NPs with these amino acids for organic transformation. In this manuscript, from the characterization, insights on the structure of these iron oxide nanoparticles with amino acids are discussed in order to understand that which type of effects can observe in the various applications by prepared iron oxide nanoparticles with different sizes, structures, and properties.

2.2 Experimental

2.2.1 Materials

Ferric chloride $FeCl_3.6H_2O$, $ZnCl_2$, and $MnSO_4$ were obtained from Loba Chemicals, India. Ferrous chloride $FeCl_2.2H_2O$ and an aqueous solution of ammonia were purchased from S.D Fine Chemicals, India. Pluronic® F-127 and L-arginine were purchased from Sigma-Aldrich. All chemicals were of AR grade and used without further purification.

2.2.2 Synthesis of L-arginine coated magnetic nanoparticles (Fe_3O_4@L-Arg NPs)

Ferric chloride hexahydrate (5.0 g, 18.5 mmol) and ferrous sulfate tetrahydrate (2.4 g, 10.7 mmol), in a molar ratio of 1:0.58, were added to 250 mL deionized water under an inert atmosphere. The mixture was heated to 70 °C to a clear solution. The mixture was stirred vigorously with a mechanical stirrer to avoid interparticle magnetic interaction. After 30 min, L-arginine (8.01 g, 46.0 mmol), dissolved in 50 mL deionized water, was rapidly added. The reaction mixture was further stirred for 30 min.

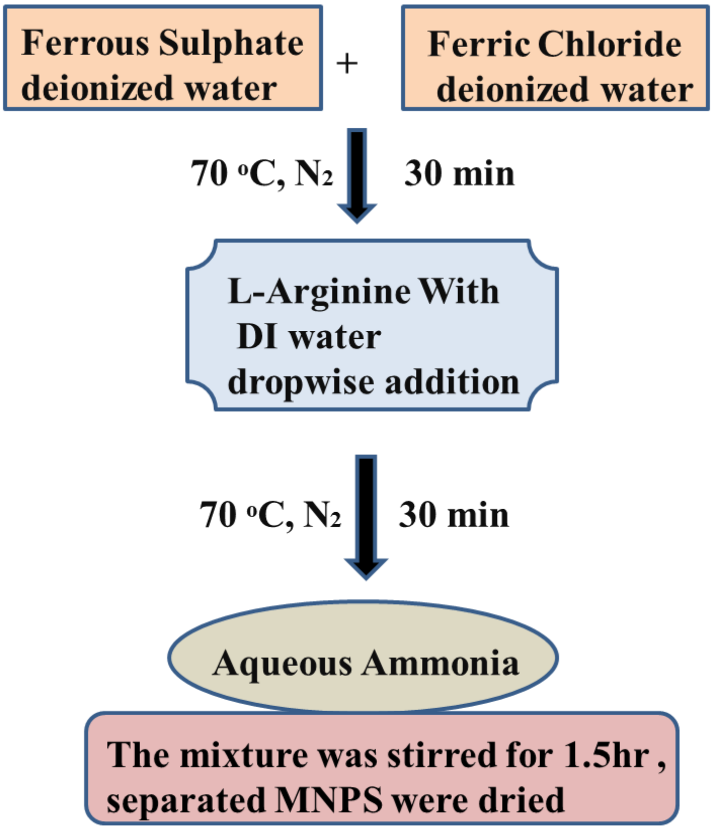

Scheme 2.1. preparation of L-arginine capped Magnetic Iron Oxide Nanoparticles Similarly, $ZnxFe_{3-x}O_4$ ($x = 0.2$)@L-arginine, $Mn_xFe_{3-x}O_4$ ($x = 0.2$)@L-arg, and $Ni_xFe_{3-x}O_4$ ($x = 0.2$)@L-arg were synthesized by adding a solution of $ZnCl_2$ (0.001 mol, 0.2689 g), $MnSO_4$ (0.001 mol, 0.151 g), and $NiCl_2$ (0.001 mol, 0.13 g) prepared in 30 mL DI water. (Scheme 2.2, Yields range from 90 to 95%).

Then 27 mL ammonia (25%) was rapidly added which, in turn, changed the reaction color to black. The stirring was continued for 1.5 h. Finally, the black nanoparticles were separated magnetically, washed with distilled water thrice, and dried at 100 °C overnight (Scheme 2.1). A dry weight of nanoparticles: 2.54 g.

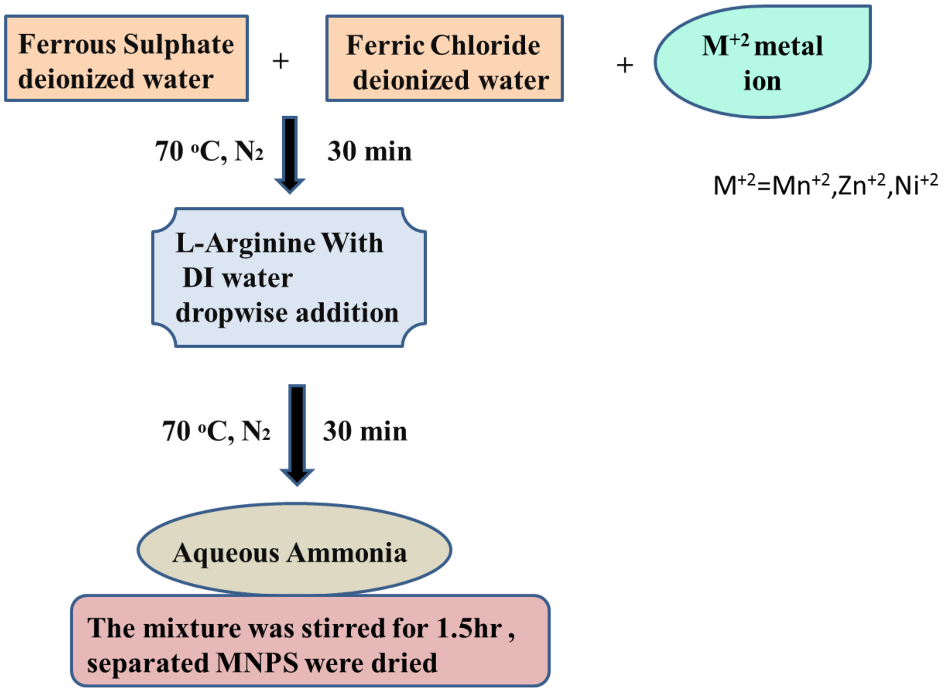

Scheme 2.2. Preparation of transition metal ions doped iron oxide nanoparticles.

2.3 Result and discussion

2.3.1 Structure and morphology elucidation

We have strategically selected L-arginine a small molecular capping ligand to arrest particle growth due to its zwitter ionic property. Out of its different resonance structures, the one having a positive charge distributed over the guanidinium nitrogen and a negative charge over the carboxylate group predominated under synthesis conditions. The negatively charged carboxylate ion can easily coordinate with the surface Fe^{2+}/ Fe^{3+} ions of Fe_3O_4 NPs rendering the overall surface hydrophilic. Now, the positively charged guanidinium group remains projected outside the surface which, in turn, orients the drug molecules around it by H-bonding. The hydrophobic part of the drug molecules forces the next Pluronic ® F127 layer to assemble in such a way that its hydrophobic PPO blocks remain tucked inward, while the hydrophilic PEO blocks on the outside form a normal hydrophilic micellar surface (Figure 2.2) [56]. It is very well recognized from previous studies that a Pluronic shell can provide a stealth outer layer to the delivery vehicle, enabling it to sustain itself while encountering all the physiological barriers through its journey into the target cells [57].

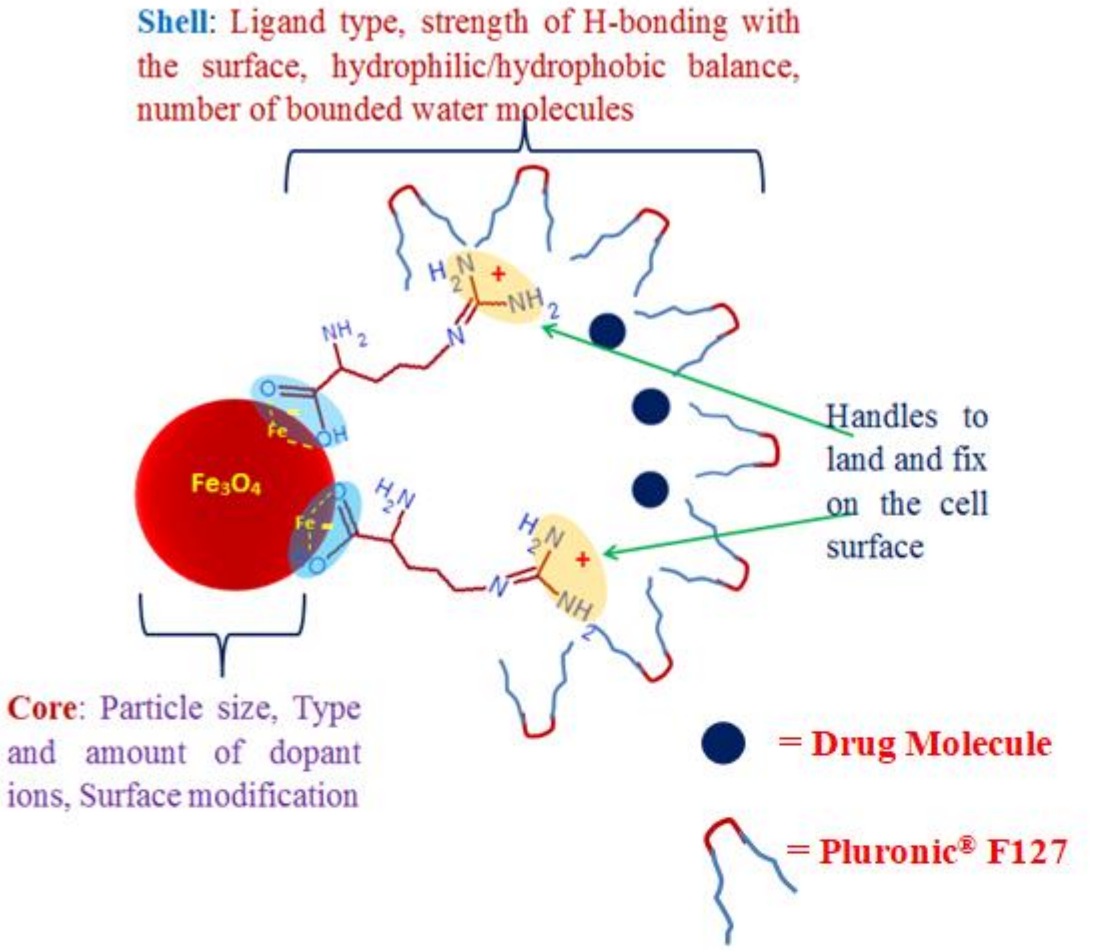

Fig. 2.2. Cartoon showing Fe_3O_4@ L-Arg/P/bg NPs magnetic micelle as a drug delivery vehicle. The parameters to tune the magnetic relaxation for MRI, enhance the drug loading and cell transfection.

L-arginine is a non-toxic amino acid and immediate precursor of NO, an important signaling molecule having a crucial function during the immune response to the infection [58].

Once inside the cell, lysosomal degradation of the assembly releases L-arginine with iron compounds. These released residues aid the function of brigatinib by inducing an immune response and thereby hastening cell apoptosis. Since L-arginine binds with brigatinib through H-bonding only during the drug loading stage, the release of the drug occurs smoothly at the target without any change in its molecular structure.

It can be seen from Figure 2.2 that the relaxation rate for $T1$ imaging can be tuned in two ways: Firstly, the particle size of the Fe_3O_4 NPs can be adjusted up to 10 nm with the magnetism tuned by doping with the suitable dopant ions.

This, in turn, can influence the dipole–dipole interactions with the inner sphere water protons relaxing faster in the presence of an applied field. Secondly, the selection of ligands for surface coordination of NPs is very important as it creates a hydrophilic shell environment by forming an inner sphere of H-bonded water molecules. The strength of H-bonding with water molecules depends on the hetero atoms present in the molecular structure of the ligand (discussed further in the Phantom study). Finally, this core@shell structure is encapsulated in a polymeric micelle formed by PEO-PPO block copolymeric surfactant, Pluronic ®F127 (during the synthesis, the amount of pluronic adjusted was above CMC, i.e., 20 mg/mL to ensure the formation of a polymeric micelle) [59]. Now, when this nano-assembly comes across the hydrophilic outer layer of the cell membrane, the Pluronic micelle can be easily engulfed into the cellular environment. In turn, when the outer micelle layer gets ruptured, the positively charged guanidinium group of L-arginine ligand acts as a handle and electrostatically interacts with the cellular surface at a proper angle to synergize the cellular transfection.

2.3.2 Crystal structure of Fe_3O_4

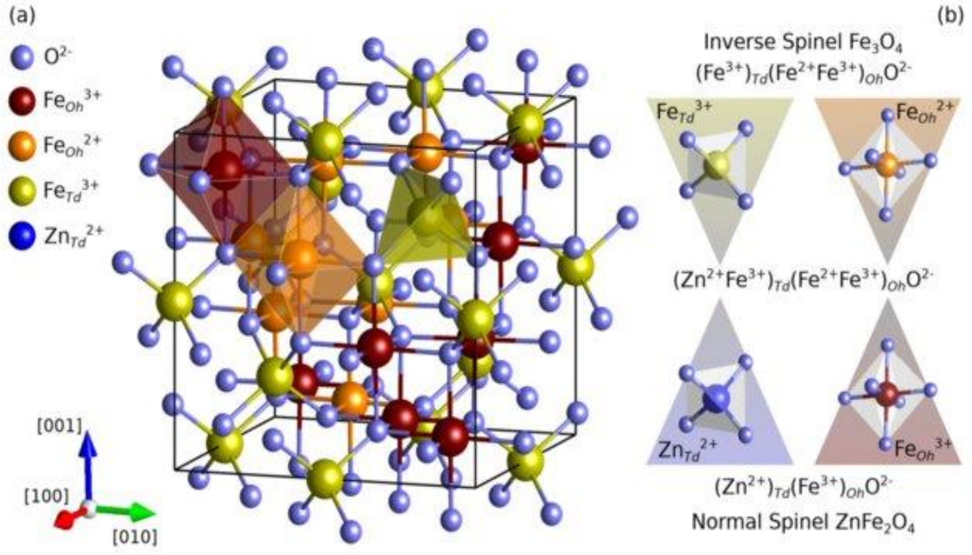

Fig. 2.3. (a) The cubic crystal structure of the inverse spinel Fe_3O_4. (b) Depiction of tetrahedral (Td) Fe^{3+} (green), Zn^{2+} (blue) and octahedral (Oh) Fe^{2+} (orange), and Fe^{3+} (red) cations, coordinated by O^{2-} (purple) anions, as well as cation distribution formula for the inverse spinel Fe_3O_4 (top), containing only Fe^{3+} Td and Fe^{2+} Oh, disordered (middle) and normal spinel $ZnFe_2O_4$ (bottom), containing Zn^{2+} Td and Fe^{3+} Oh cations.

2.3.3 Powder X-ray Diffraction(PXRD)

From the XRD pattern (Figure 2.4 & 2.5) it can be observed that dopant ions do not affect the phase purity of the material or induce any strain. The diffraction peaks at 2θ values 30.1, 35.25, 43.15, 53.67, 57.32, and 63.16 correspond to (200), (311), (400), (422), (511) and (440) planes (JCPDS 82-1533) respectively. This pattern is a signature of an inverted spinel structure with the magnetite phase of iron oxide NPs. The particle size of all the samples was calculated by using the Debye–Scherrer formula ($L = 0.9\ \lambda/\beta\cos\theta$) [60].

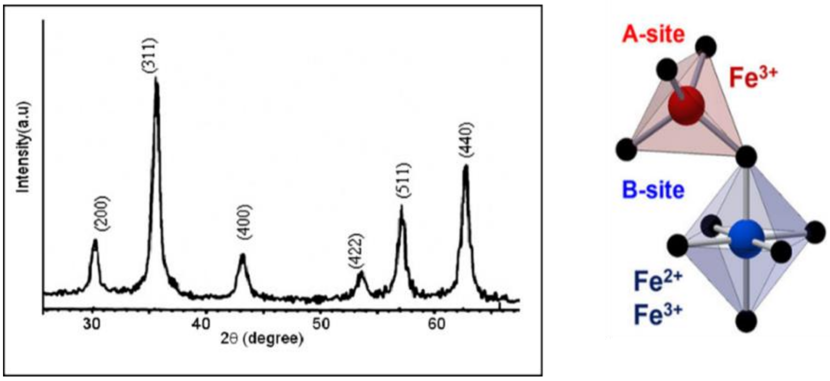

Fig. 2.4. XRD pattern of the as-synthesized Fe_3O_4@L-Arg nanoparticles**.**

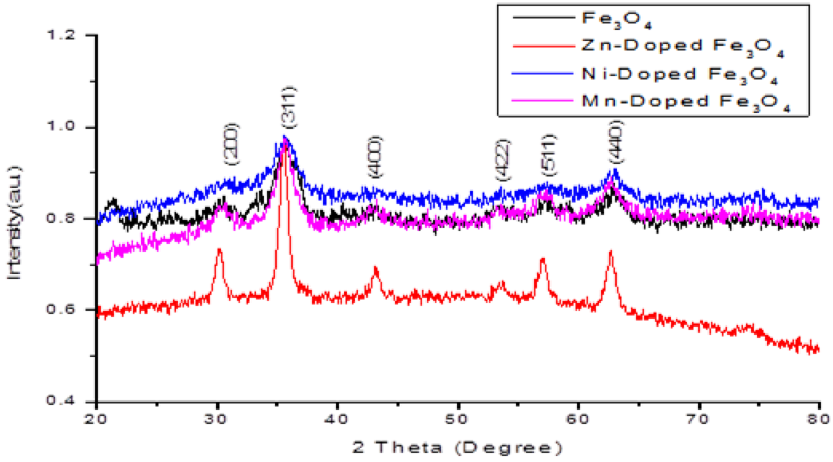

Fig. 2.5. XRD pattern of the as-synthesized M^{2+}/Fe_3O_4@L-Arg nanoparticles.

The dopant does not form a new phase, detectable by XRD, which can adversely affect the magnetic property of the material. It is well known that the location of dopant ions in ferrimagnetic inverted spinel material is crucial as it influences the magnetic moment of the material.

2.3.4 High-Resolution Transmission Electron Microscopy (HRTEM) analysis

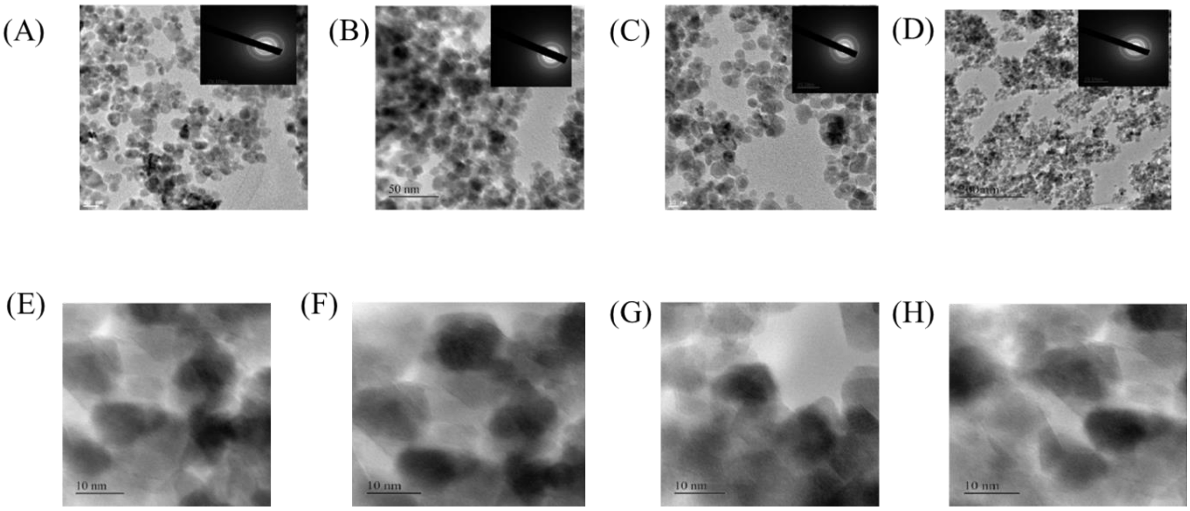

Fig. 2.6. (i) A–D HRTEM images (inset image shows SAED pattern),(ii)E–H HRTEM lattice fringes at higher magnification of as-synthesized blank, Zn^{2+}, Mn^{2+}, and Ni^{2+}/ Fe_3O_4@L-Arg/P NPs, respectively.

The morphology of the samples was examined by Transmission Electron Microscopy (TEM, Philips Tecnai 20) at 200 kV. All measurements were taken at 25 °C in deionized water. Further, the size and shape of M^{2+}/Fe_3O_4@L-Arg/P NPs were studied by High-Resolution Transmission Electron Microscopy (HRTEM) analysis. The HRTEM images show spherical particles, and the size histograms reveal 10–12 nm particle size. The SAED patterns show the polycrystalline nature of the material Figure 2.6.

2.4 Characterization

2.4.1 FTIR Spectroscopy

The mode of interaction of L-arginine with the surface Fe ions of Fe_3O_4 NPs was studied by using Fourier Transform Infrared Spectroscopy (RX-FTIR, Perkin-Elmer, USA).

The interaction of L-arginine with Fe_3O_4 NPs surface was studied by FTIR spectroscopy (Figure 2.7). Free carboxylate ions in acetate form vibrate in two fundamental modes: asymmetric $\nu_{as}(COO^-)$ and symmetric ν_s (COO^-) stretching at 1583 and 1422 cm^{-1}, respectively. In the case of Fe_3O_4@L-arg NPs, the $\nu_{as}(COO^-)$ = 1645 cm^{-1} and ν_s (COO^-) =

1390 cm^{-1} obtained. Hence, in coordination with surface Fe ions, ν_{as} (COO^-) increases, while ν_s(COO^-) decreases, indicating monodentate coordination of the carboxylate ion of amino acid. Also, Δ ($\nu_{as}(COO^-) - \nu_s(COO^-)$) < Δ' ($\nu_{as}(COO^-) - \nu'_s(COO^-)$), where Δ is the difference in the absorption bands for free carboxylate ions and Δ' for metal-bound carboxylate ions, suggesting monodentate coordination [61-63]. The absorption at 646 cm^{-1} corresponds to Fe–O stretching in the Fe_3O_4 inverse spinel system. Absorptions at 1111 cm^{-1} and 1156 cm^{-1} are due to the presence of the block copolymer completely encapsulating the NPs surface and –CH_2 rocking vibration of Pluronic, respectively [64].

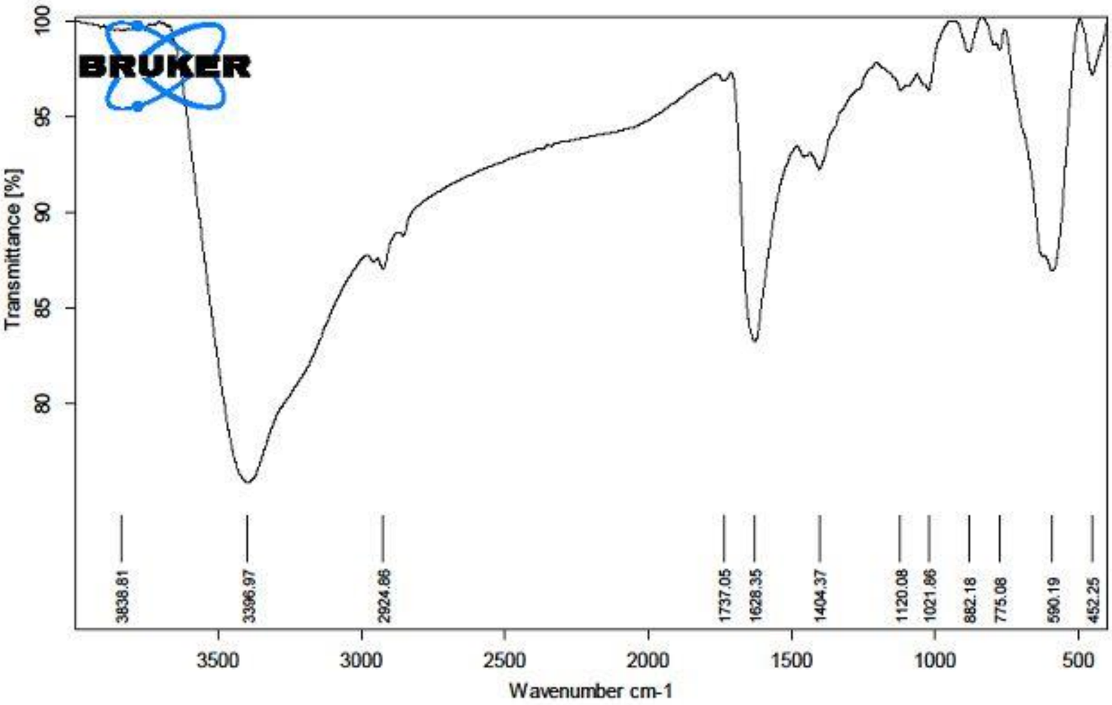

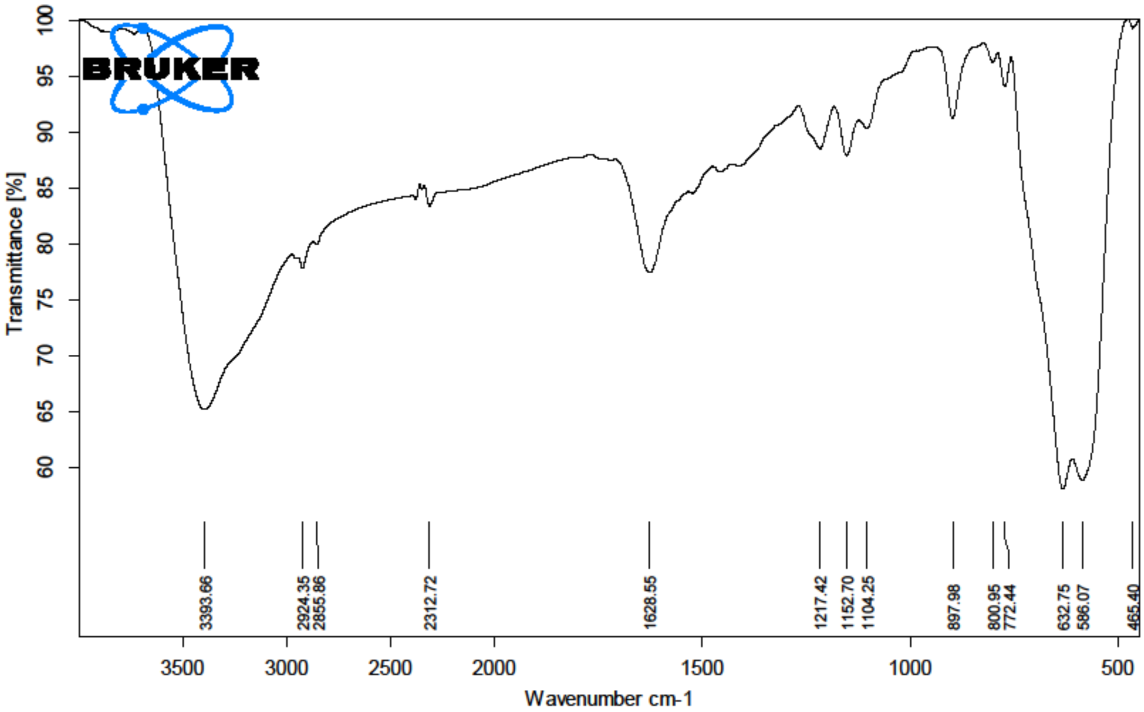

Fig. 2.7. FTIR Spectra of as-synthesized Fe_3O_4@L-Arg and Fe_3O_4@L-Arg/P

2.4.2 Powder XRD Study (FWHM)

Table 1. Calculation of particle size of Fe_3O_4@L-arg from FWHM values obtained from XRD.

Fe_3O_4@L-arg				
Sr. No.	**2 Theta Position**	**FWHM**	**Size (nm)**	**Average Size (nm)**
1	21.24287	0.96323	**8.77**	(8.77 + 6.75 + 4.38 + 14.05 + 8.14 + 5.27)/6 = 47.36/ 6 = **7.89**
2	30.39103	1.27508	**6.75**	
3	35.92013	1.9933	**4.38**	
4	53.18411	0.6606	**14.05**	
5	57.26783	1.16152	**8.14**	
6	62.98694	1.84707	**5.27**	

Table 2. Calculation of particle size of Ni^{2+}/Fe_3O_4@L-arg from FWHM values obtained from XRD

		Ni^{2+}/Fe_3O_4@L-arg		
Sr. No.	**2 Theta Position**	**FWHM**	**Size (nm)**	**Average Size (nm)**
1	35.59869	2.31048	**3.93**	(3.93 + 2.5 + 1.75 + 4.11)/4 = 12.29/ 4 = **3.0725**
2	43.24721	3.56637	**2.5**	
3	56.95942	5.39117	**1.75**	
4	62.89986	2.36859	**4.11**	

Table 3. Calculation of particle size of Mn^{2+}/Fe_3O_4@L-arg from FWHM values obtained from XRD

		Mn^{2+}/Fe_3O_4@L-arg		
Sr. No.	**2 Theta Position**	**FWHM**	**Size (nm)**	**Average Size (nm)**
1	30.39526	1.2957	**6.64**	(6.64 + 5.1 + 4.42 + 5.31 + 6.41 + 4.38)/6 = 32.26/ 6 = **5.376**
2	35.62933	1.70922	**5.1**	
3	43.08722	2.01864	**4.42**	
4	53.65635	1.75113	**5.31**	
5	57.17535	1.47583	**6.41**	
6	62.6716	2.21736	**4.38**	

Table 4. Calculation of particle size of Zn^{2+}/Fe_3O_4@L-arg from FWHM values obtained from XRD

Zn^{2+}/Fe_3O_4@L-arg				
Sr. No.	**2 Theta Position**	**FWHM**	**Size (nm)**	**Average Size (nm)**
1	30.16543	0.86	**10**	(10 + 10.01 + 14.32 + 12.22 + 9.81 + 8.9 + 5.39)/7 = 70.65/ 7 = **10.09**
2	35.5273	0.87066	**10.01**	
3	43.15688	0.62343	**14.32**	
4	53.53732	0.76101	**12.22**	
5	57.04529	0.96275	**9.81**	
6	62.68145	1.09165	**8.9**	
7	74.20635	1.93021	**5.39**	

The FWHM values of the major XRD planes are in the range of 5–12 nm.

2.4.3 Energy-dispersive X-ray Analysis (EDAX)

Fe_3O_4@L-Arg

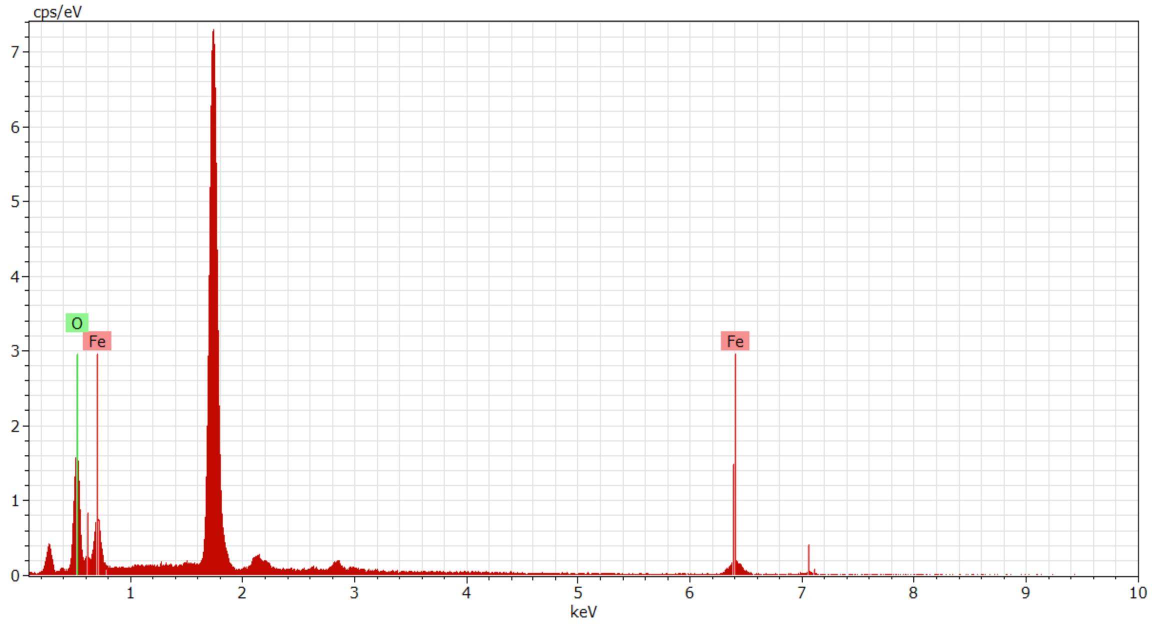

Fig. 2.8. EDS analysis of as-synthesized Fe_3O_4@L-Arg NPs

```
Element  Series  unn. C norm. C Atom. C Error (3 Sigma)
[wt.%]  [wt.%]  [at.%]         [wt.%]
-----------------------------------------------------
Iron    K-series  34.52   76.52   48.28           5.69
Oxygen  K-series  10.59   23.48   51.72           4.95
-----------------------------------------------------
Total:  45.12  100.00  100.00
```

Zn^{2+}/Fe$_3$O$_4$@L-Arg

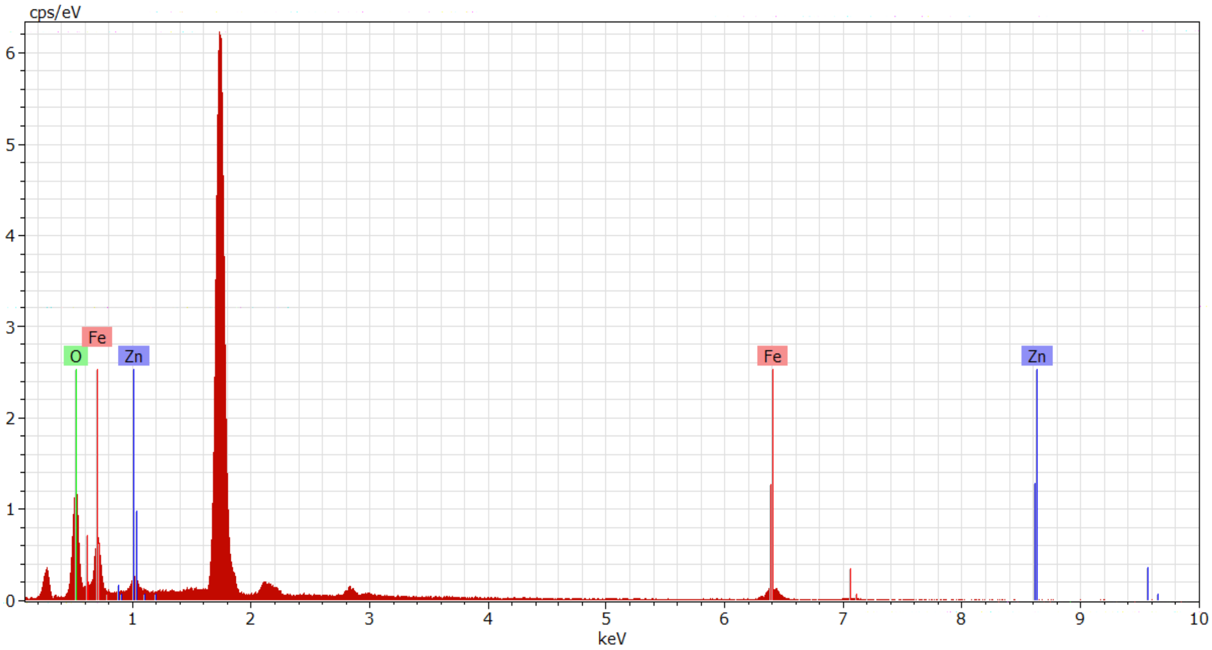

Fig. 2.9. EDS analysis of as-synthesized Zn^{2+}/Fe$_3$O$_4$@L-Arg NPs

```
Element  Series  unn. C norm. C Atom. C Error (3 Sigma)
               [wt.%]  [wt.%]  [at.%]         [wt.%]
-----------------------------------------------------
Oxygen  K-series  11.23   22.19   50.30           5.15
Iron    K-series  34.94   69.04   44.84           5.66
Zinc    L-series   4.44    8.77    4.87           1.05
-----------------------------------------------------
        Total:  50.61  100.00  100.00
```

Ni^{2+}/Fe$_3$O$_4$@L-Arg

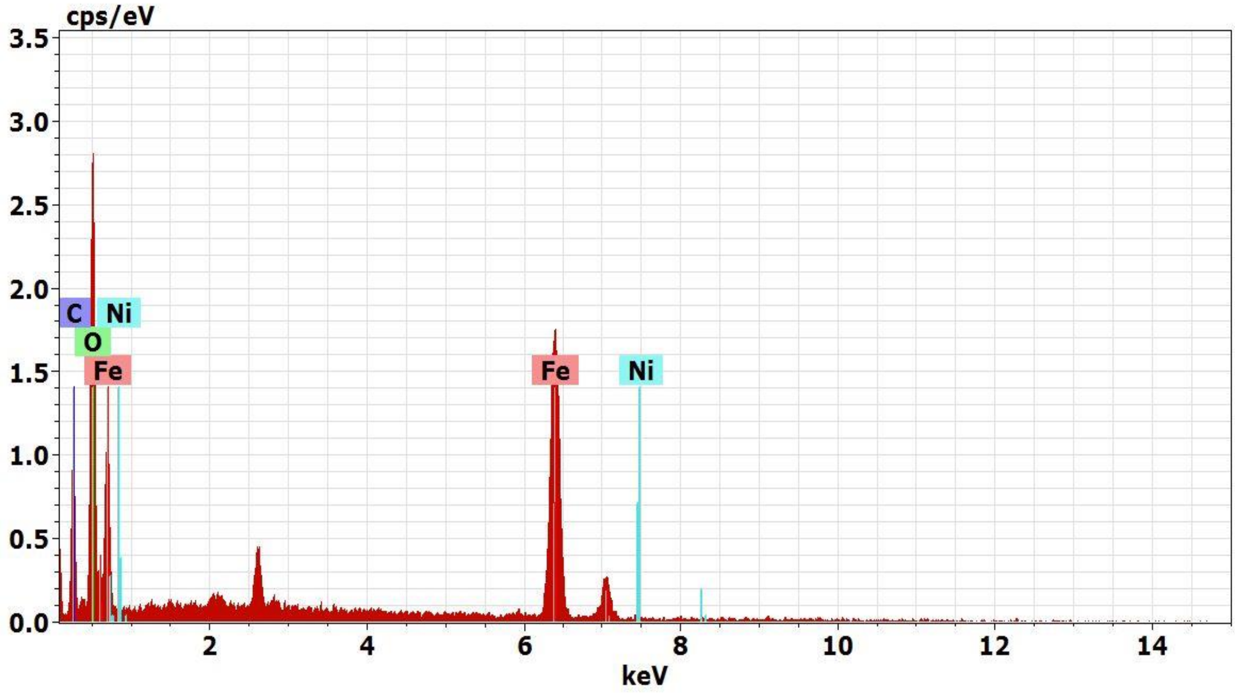

Fig. 2.10. EDS analysis of as-synthesized Ni^{2+}/Fe$_3$O$_4$@L-Arg NPs

```
Element  Series  unn. C norm. C Atom. C Error (3 Sigma)
                 [wt.%]  [wt.%]  [at.%]        [wt.%]
-----------------------------------------------------
Iron    K-series  66.55   61.22   28.77          6.62
Oxygen  K-series  24.83   22.84   37.47          12.51
Carbon  K-series  16.67   15.33   33.50          10.97
Nickel  K-series   0.65    0.60    0.27          0.42
-----------------------------------------------------
         Total: 108.70  100.00  100.00
```

Mn^{2+}/Fe_3O_4@L-Arg

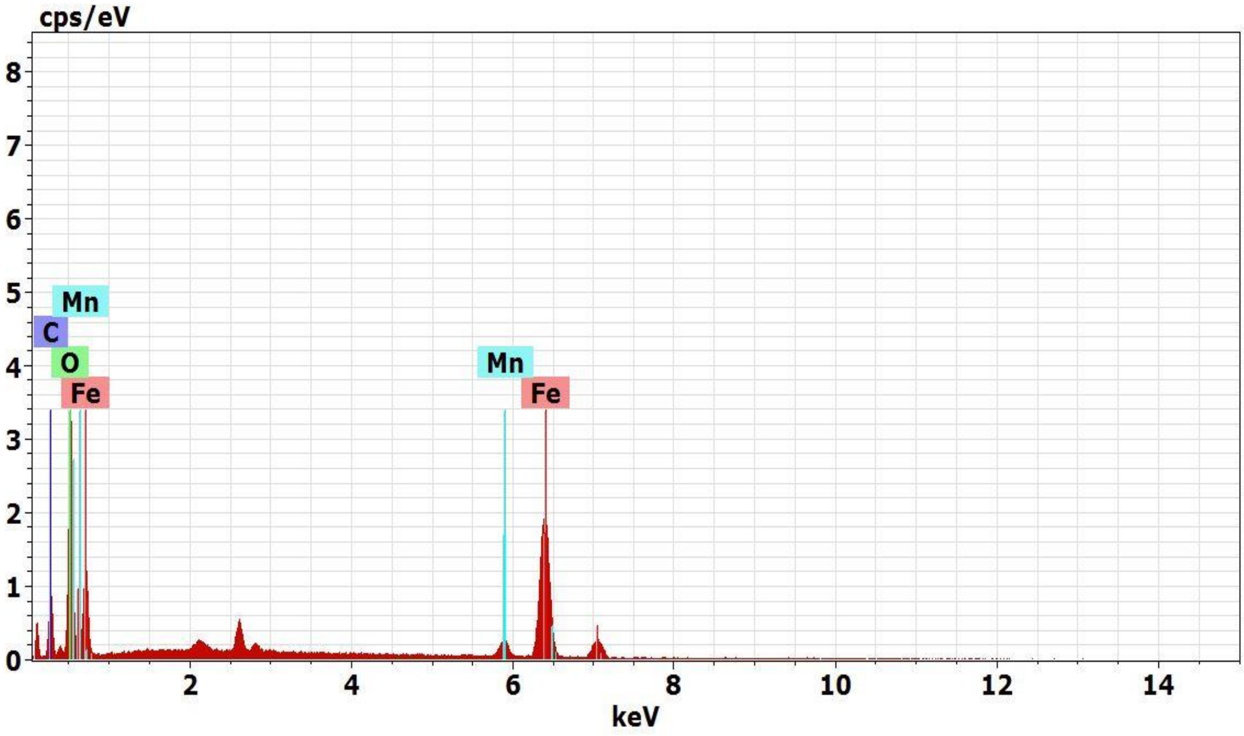

Fig. 2.11. EDS analysis of as-synthesized Mn^{2+}/Fe_3O_4@L-Arg NPs

Element	Series	unn. C [wt.%]	norm. C [wt.%]	Atom. C [at.%]	Error (3 Sigma) [wt.%]
Iron	K-series	61.09	60.62	30.61	5.62
Oxygen	K-series	22.00	21.83	38.47	8.97
Carbon	K-series	12.04	11.95	28.05	6.25
Manganese	K-series	5.65	5.61	2.88	0.69
	Total:	100.79	100.00	100.00	

2.4.4 VSM Analysis:

In an inverted spinel structure of magnetite, the Fe^{3+} ions present at A sites are anti-ferromagnetically coupled with those present in equal numbers at B sites and cancel the overall magnetism generated due to Fe^{3+} ions. Hence, only Fe^{2+} ions present at B sites are responsible for the observed magnetic property [65]. Now, the dopant ions (in the M^{2+} state) have a preference for the particular interstitial sites which depends on the reaction parameters adopted during the synthesis of the material. Cu^{2+}, Ni^{2+}, and Co^{2+} prefer Oh sites and replace Fe^{2+} ions, resulting in net magnetic moments 1, 2, and 3 μ_B respectively [66]. This enhanced magnetic moment increases r_2 relaxivity during the MR. Surprisingly, Mn^{2+} and Zn^{2+} ions have a preference for Td sites and the overall magnetic moment is affected by their distribution as well as oxidation state (may be changed during synthesis to Mn^{3+}, and Mn^{4+}) [67]. On the contrary, the substitution of Fe^{2+} at the Oh sites by Zn^{2+} ions increases the magnetic moment at lower doses while the higher doses (> 0.4) favor antiferromagnetic interactions and decrease the magnetic moment [68].

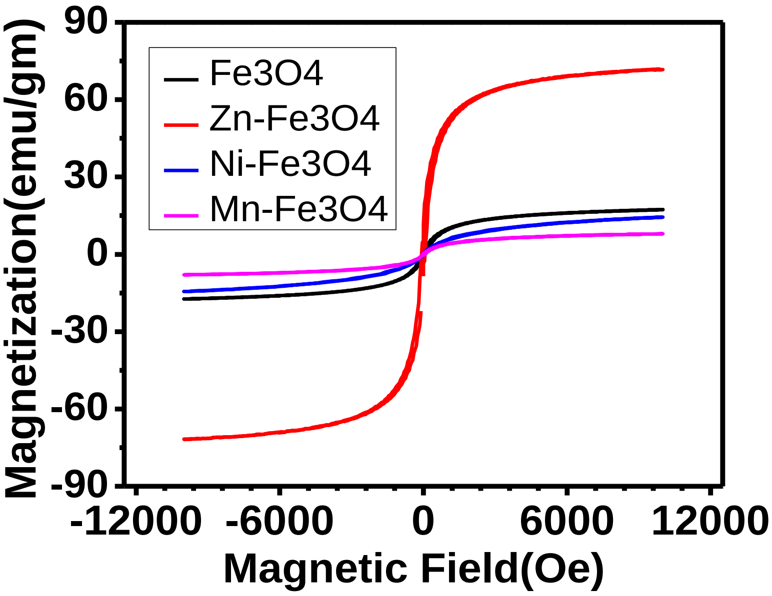

Fig. 2.12. Effect of doping on the magnetic properties of the material studied by VSM analysis.

The substitution of Fe^{2+} at the Oh sites by Zn^{2+} ions increases the magnetic moment at lower doses, while the higher doses (>0.4) favour antiferromagnetic interactions and decrease the magnetic moment. The effect of doping on the magnetic properties of the material was studied by VSM analysis (Figure 2.12). From the M-H curves, it can be observed that blank Fe_3O_4 NPs exhibit paramagnetic behaviour with less Ms value (30.1 emu/g), while on Zn^{2+} doping, it increases to 72.5 emu/g. Generally, in the bulk form, blank Fe_3O_4 has a Ms value of 80–90 emu/g and it increases upon transforming into a nanoregime [69-70].

However, the less Ms value, in the present case, indicates surface spin randomness at very small particle size. The enhancement in Ms value on Zn^{2+} doping corroborates the Mössbauer results. On the other hand, Mn^{2+} and Ni^{2+}doping retains the paramagnetic behavior of the material due to the very less particle size [71].

2.4.5 Mössbauer Spectroscopy

The location of dopant ions, their interaction with the surrounding as well as their oxidation states play critical role in functioning of the catalyst. Mössbauer spectroscopy is one of the tools to reveal local composition and structure of the catalyst as well as oxidation state of Fe present as dopant ions in host. The perturbation in the local environment due to dopants can be very well detected by this technique. The Mossbauer spectroscopy of all the synthesized samples was carried out at RT (300 K), and the results are shown in Table 5.

Table 5. Room temperature Mössbauer spectral data of as-synthesized M^{2+}/Fe_3O_4@L-Arg/P NPs.

NPs Sample	**Magnetic Field (kOe)**		**Q.S. in mm/s**	**I.S. mm/sec**			**Area under curve (%)**			**Saturation magnetization M_s (emu/g)**
	A	B	C	A	B	C	A	B	C	
Fe_3O_4@L-Arg/P	-	-	0.64 (0.02)	-	-	0.36 (0.02)	-	-	1.00	29.8
Ni^{2+}/Fe_3O_4@L-Arg/P	484 (3.2)	428 (3.2)	-	0.39 (0.02)	0.55 (0.02)	0.38 (0.02)	66.3	33.7	-	14.0
Mn^{2+}/Fe_3O_4@L-Arg/P	488 (3.2)	-	0.64 (0.02)	0.17 (0.02)	-	0.33 (0.02)	58.8	-	41.2	8.0
Zn^{2+}/Fe_3O_4@L-Arg/P	-	426.8 (3.2)	0.64 (0.02)	-	0.40 (0.02)	0.32 (0.02)	-	68.4	31.6	72.5

It can be observed that the Fe^{2+}/Fe^{3+} ions in the blank Fe_3O_4 could not couple with each other confirming the paramagnetic nature. This is due to the spin canting effect predominant at very small particle sizes. On doping Mn^{2+} ions, the hyperfine interaction comes into existence at the A sites while the Fe ions present at the B sites remain inactive. This is due to Mn^{2+}ions substituting Fe^{2+} at Oh sites perturbing the local environment to make Fe ions couple with each other through oxygen atoms. This results in a hyperfine splitting of energy levels at A sites while no change in the local environment at B sites. On the contrary, Zn^{2+} ions doping substitutes Fe^{2+}/Fe^{3+} at Oh sites, and in turn, hyperfine splitting can be observed at B sites while the Fe^{3+}ions at A sites remain silent [72]. Interestingly, Ni^{2+} ions get engaged at both the sites, which results in super exchange interaction among Fe^{3+} ions at Td and Oh sites while interaction among Fe ions at Oh sites lead to double exchange interaction. These generate sextuplets in Mössbauer spectra [73-74].

2.4.6 Thermal analysis

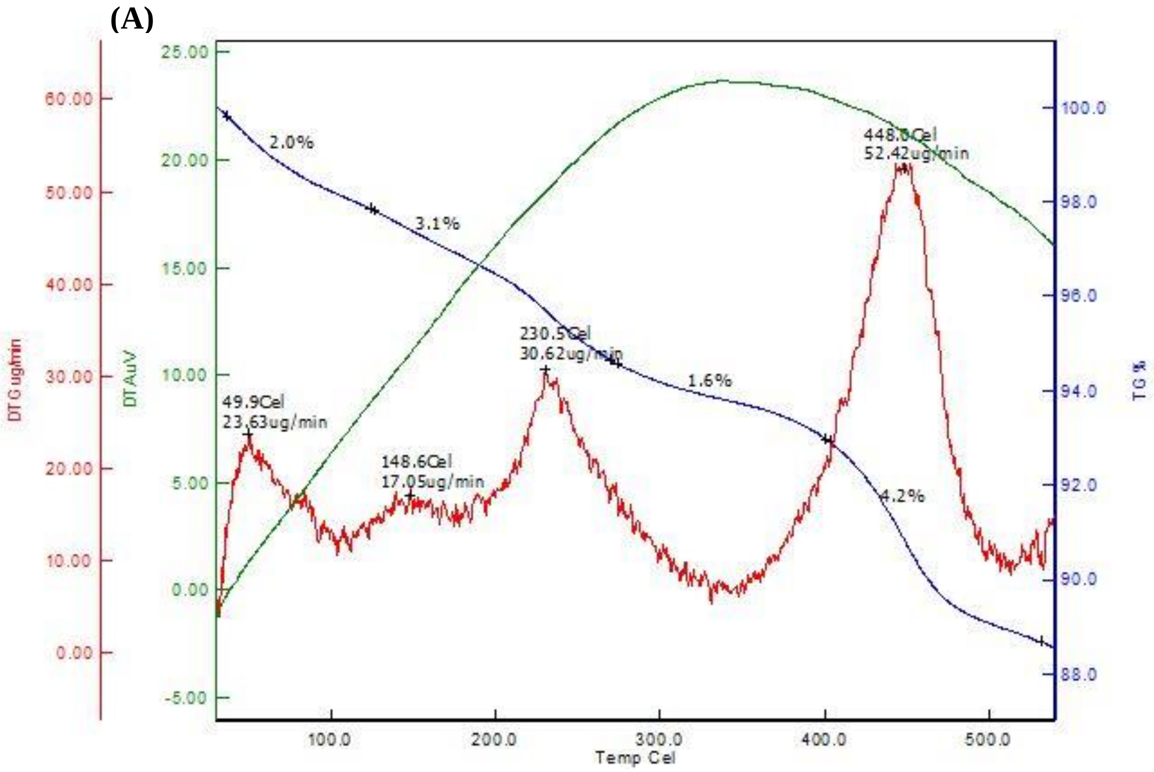

(B)

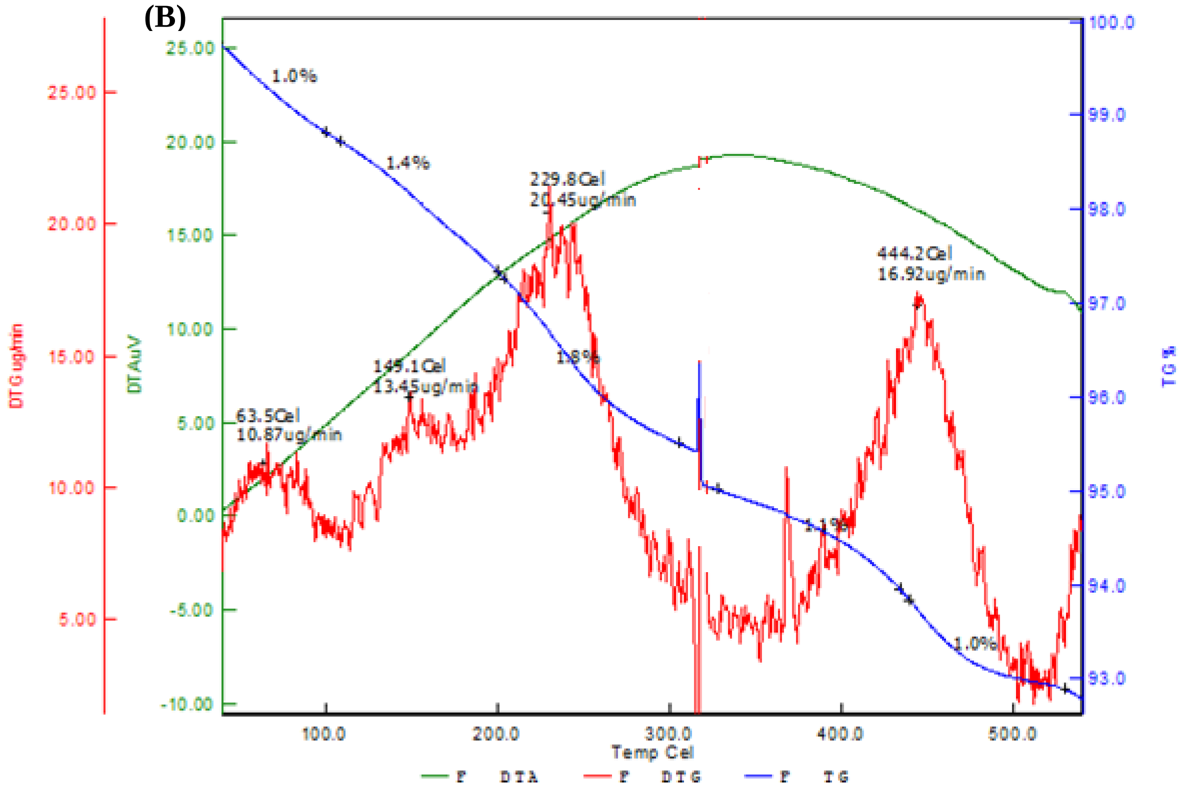
DTG ug/min
25.00
20.00
15.00
10.00
5.00
DTA uV
25.00
20.00
15.00
10.00
5.00
0.00
-5.00
-10.00
TG %
100.0
99.0
98.0
97.0
96.0
95.0
94.0
93.0
1.0%
1.4%
229.8Cel
20.45ug/min
444.2Cel
16.92ug/min
145.1Cel
13.45ug/min
1.8%
63.5Cel
10.87ug/min
1.1%
1.0%
100.0
200.0
300.0
400.0
500.0
Temp Cel
F DTA
F DTG
F TG

(C)

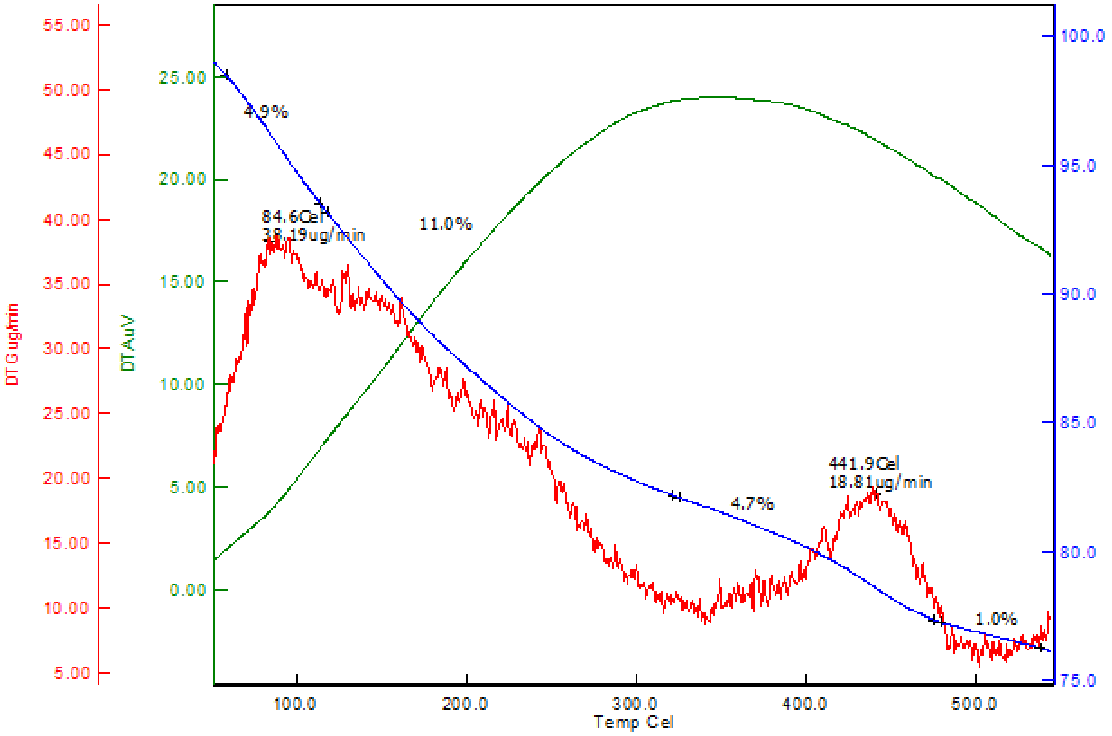
DTG ug/min
55.00
50.00
45.00
40.00
35.00
30.00
25.00
20.00
15.00
10.00
5.00
DTA uV
25.00
20.00
15.00
10.00
5.00
0.00
TG %
100.0
95.0
90.0
85.0
80.0
75.0
4.9%
84.6Cel
38.19ug/min
11.0%
441.9Cel
18.81ug/min
4.7%
1.0%
100.0
200.0
300.0
400.0
500.0
Temp Cel

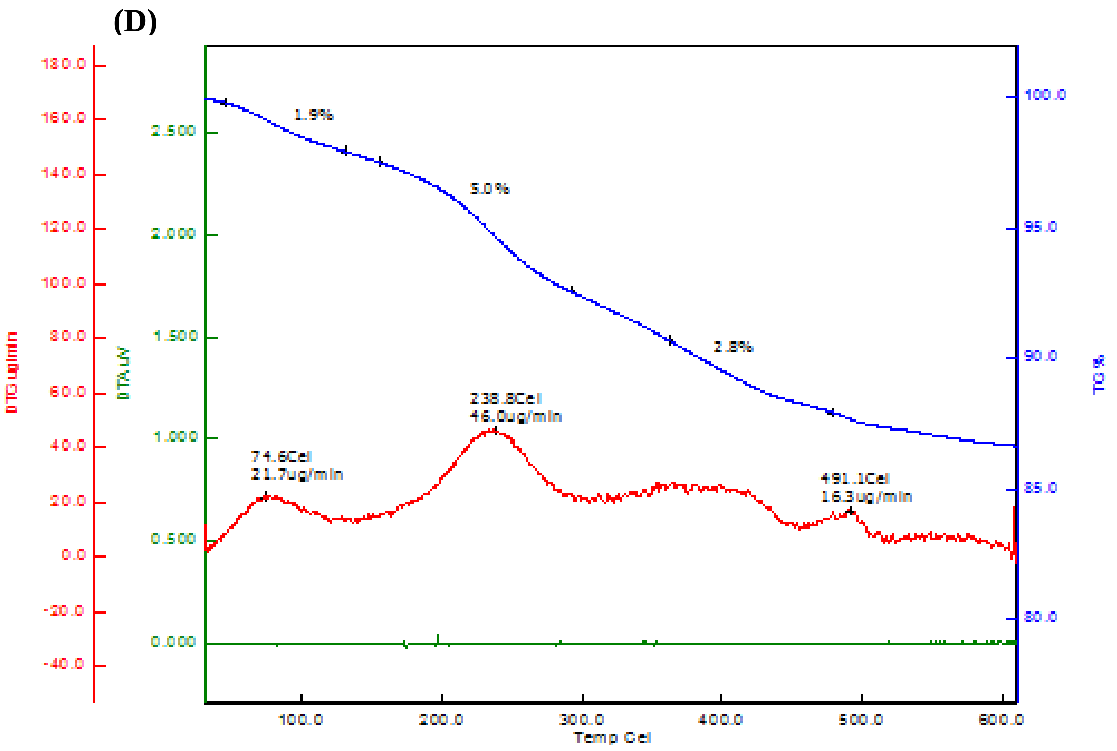

Fig. 2.13. Thermal analysis of (A) Fe_3O_4@ L-Arg/P (B) Ni^{2+}/ Fe_3O_4@L-Arg/P (C) Mn^{2+}/ Fe_3O_4@L-Arg/P, and (D) Zn^{2+}/ Fe_3O_4@L-Arg/P NPs

Moreover, the successful encapsulation of NPs surfaces by the Pluronic-F127 layer was also confirmed by the thermal analyses. To evaluate the presence of inner sphere H-bonded water in the shell environment, a thermal analysis of all the samples was carried out (Figure. 2.13). It can be observed from the thermograms that all the samples except Zn^{2+}/ Fe_3O_4@L-Arg/P exhibit two kinds of weight loss in the range of 50–85 and around 150 °C due to bulk and interior surface-bound water, respectively. The weight loss above 100 °C is continued and persisted till 150 °C, confirming the presence of inner sphere H-bonded water. The weight losses at higher temperatures are due to the carbonization of organic material, confirming the presence of a Pluronic layer at the outer shell. Hence, it can be claimed that the $r1$ relaxivity of the bulk water protons can be raised by H-bonded water molecules present near the core of magnetic NPs.

2.5 Conclusion

L-arginine capped and transition metal ions (Zn^{2+}, Mn^{2+}, and Ni^{2+}) doped Fe_3O_4 nanoparticles are successfully synthesized by wet chemical methods. As-synthesized nanoparticles were characterized by various techniques.

(i) FTIR spectroscopy confirms the way of interaction of amino acid molecules with the surface of the nanoparticles.

(ii) The purity of the phase and lattice structure of doped and undoped nanoparticles were studied by XRD and Mossbauer spectroscopy. The particle size calculated by FWHM values derived from XRDs were in the nano regime. It confirms that there is a negligible effect of doping on particle size of as-synthesized magnetite.

(iii) Successful doping of the transition metal ions was also confirmed by elemental analysis.

(iv) Particle size and shape were also studied by TEM analysis.

(v) VSM analysis nicely explains the variation in magnetic properties of the material on doping.

(vi) The as-synthesized nanoparticles were coated with Pluronic®F127.

The resulting magnetic micelle was acted as drug delivery carrier. Moreover, the successful encapsulation of NPs surfaces by the Pluronic-F127 layer was also confirmed by the thermal analyses.

2.6 References

1. Lodhia, J. Mandarano, G. Ferris, N.; Eu, P.; Cowell, S., Biomed. Imaging Interv. J., 6, 12, (2010).
2. Dhak, P.; Kim, M.-K.; Lee, J.H.; Kim, M.; Kim, S.-K., J. Magn. Magn. Mater., 433, 47, (2017).
3. Sivula, K.; Le Formal, F.; Grätzel, M., ChemSusChem., 4, 432, (2011).
4. Cornell, R.M.; Schwertmann, U., VCH: Weinheim, Germany, (2003).
5. M. U. Muckenthaler, S. Rivella, M. W. Hentze, B. Galy, Cell., 168, (2017).
6. L. Chen, D. A. Bazylinski, B. H. Lower, Nature Education Knowledge, 3, 30, (2010).
7. How Do Birds Navigate? STEMvisions Blog, By Science and Technology Concepts Middle School, 4 Jan, 2020.
8. ACS Molecule of the Week Archive: Magnetite, June 15, (2020).
9. L. C. Naisbett-Jones, N. F. Putman, M. M. Scanlan, D. L. G. Noakes, K. J. Lohmann, J. Exp. Biol., 223, (2020).
10. W. Wei, C. Z. Jiang, V. A. L. Roy, Nanoscale., 8, 19421, (2016).
11. E. -K. Lim, T. Kim, S. Paik, S. Haam, Y. –M. Huh, K. Lee, Chem. Rev., 115, 327, (2015).
12. J. Chomoucka, J. Drbohlavova, D. Huska, V. Adam, R. Kizek, J. Hubalek, Pharmacol. Res., 62, 144, (2010).
13. Z. R. Lu, P. Qiao, Drug Delivery in Cancer Therapy, Quo Vadis? Mol. Pharmaceutics., 15, 3603, (2018).
14. D. Yoo, J. –H. Lee, T. –H. Shin, J. Cheon, Acc. Chem. Res., 44, 863, (2011).
15. M. Soleymani, S. Khalighfard, S. Khodayari, H. Khodayari, M. R. Kalhori, M. R. Hadjighassem, Z. Shaterabadi, A. M. Alizadeh, Sci. Rep., 10, 1695, (2020).
16. R. J. Mannix, S. Kumar, F. Cassiola, Montoya-Zavala, M.; Feinstein, E.; Prentiss, M.; Ingber, Nat. Nanotechnol., 3, 36, (2008).
17. J. Dobson, Nat. Nanotechnol., 3, 139, (2008).
18. M. U. Muckenthaler, S. Rivella, M. W. Hentze, B. Galy, Cell, 168, 344, (2017).
19. N. Lee, T. Hyeon, Chem. Soc. Rev. 41, 2575, (2012).
20. R. C. O’Handley, WileyInterscience, New York (1999).
21. J. W. M. Bulte, D. L. Kraitchman, NMR Biomed., 17, 484, (2004).
22. B. D. Cullity, Introduction to magnetic materials, Addision Wesley Pub. Company, Reading, MA (1972).

23. Q. A. Pankhurst, J. Connolly, S. K. Jones, J. Dobson, J. Phys. D: Appl. Phys., 36, R161, (2003).
24. U. Jeong, X. Teng, Y. Wang, H. Yang, Y. Xia, Adv. Mater., 19, 33, (2007).
25. Y. S. Kang, S. Risbud, J. F. Rabolt, P. Stroeve, Chem. Mater. 8, 2209, (1996).
26. X. K. Zhao, P. J. Horve, J. H. Fendler, J. Phys. Chem., 93, 908, (1989).
27. F. C. Meldrum, N. A. Kotov, J. H. Fendler, J. Phys. Chem., 98, 4506, (1994).
28. S. V. Salihov, Y. A. Ivanenkov, S. P. Krechetov, M. S. Veselov, N. V. Sviridenkova, A. G. Savchenko, N. L. Klyachko, Y. I. Golovin, N. V. Chufarova, E. K. Beloglazkina, A. G., J. Magn. Magn. Mater., 394, 173, (2015).
29. T. Hyeon, Chemical synthesis of magnetic nanoparticles, Chem. Commun., 927, (2003).
30. X. Wang, R. D. Tilley, J. J. Watkins, Langmuir, 30, 1514, (2014).
31. Bhavani, P.; Rajababu, C.; Arif, M.; Reddy, I.V.S.; Reddy, N.R., J. Magn. Magn. Mater., 426, 459, (2017).
32. De Tercero, M.D.; Bruns, M.; Martínez, I.G.; Türk, M.; Fehrenbacher, U.; Jennewein, S.; Barner, L., Part. Part. Syst. Charact., 30, 229, (2013).
33. Takami, S.; Sato, T.; Mousavand, T.; Ohara, S.; Umetsu, M.; Adschiri, T., Mater. Lett., 61, 4769, (2007).
34. Ge, S.; Shi, X.; Sun, K.; Li, C.; Uher, C.; Baker, J.R., Jr.; Banaszak Holl, M.M.; Orr, B.G., J. Phys. Chem. C, 113, 13593, (2009).
35. Li, J.; Shi, X.; Shen, M., Part. Syst. Charact., 31, 1223, (2014).
36. Zeng, P.; Zhao, Y.; Lin, Y.; Wang, X.; Li, J.; Wang, W.; Fang, Z., Res. Lett., 12, 13, (2017).
37. Cabrera, L.; Gutierrez, S.; Menendez, N.; Morales, M.; Herrasti, P., Electrochimica Acta, 53, 3436, (2007).
38. Okoli, C.; Sanchez-Dominguez, M.; Boutonnet, M.; Järås, S.; Civera, C.; Solans, C.; Kuttuva, G.R., Langmuir, 28, 8479, (2012).
39. Lopez-Perez, J.; Lopez-Quintela, M.; Mira, J.; Rivas, J. IEEE Trans. Magn., 33, 4359, (1997).
40. Basak, S.; Chen, D.-R.; Biswas, P. Chem. Eng. Sci., 62, 1263, (2007).
41. Vijayakumar, R.; Koltypin, Y.; Felner, I.; Gedanken, A. Sonochemical., Mater. Sci. Eng. A., 286, 101, (2000).
42. Hassanjani-Roshan, A.; Vaezi, M.R.; Shokuhfar, A.; Rajabali, Z., Particuology, 9, 95, (2011).

43. Gonzalez-Moragas, L.; Yu, S.-M.; Murillo-Cremaes, N.; Laromaine, A.; Roig, A., Chem. Eng. J. 281, 87, (2015).
44. Lastovina, T.A.; Budnyk, A.P.; Soldatov, M.A.; Rusalev, Y.V.; Guda, A.A.; Bogdan, A.S.; Soldatov, A.V., Mendeleev Commun., 27, 487, (2017).
45. Bonfim, L.; Passos, P.D.Q.S.; Gonçalves, K.D.O.; Courrol, L.C.; Silva, F.R.D.O.; Vieira, D.P. Appl. Nanosci., 9, 1707, (2019).
46. Singh, M.; Ulbrich, P.; Prokopec, V.; Svoboda, P.; Šantavá, E.; Štˇepánek, F.. J. Solid State Chem., 200, 150, (2013).
47. Lin, L.; Starostin, S.A.; Hessel, V.; Wang, Q. Chem. Eng. Sci., 168, 360, (2017).
48. Lakshminarayanan, S.; Shereen, M.F.; Niraimathi, K.L.; Brindha, P.; Arumugam, Sci. Rep., 11, 8643, (2021).
49. Priya; Naveen; Kaur, K.; Sidhu, A.K. Green Synthesis. Front. Nanotechnol., 3, 655062, (2021).
50. Bibi, I.; Nazar, N.; Ata, S.; Sultan, M.; Ali, A.; Abbas, A.; Jilani, K.; Kamal, S.; Sarim, F.M.; Khan, M.I.; et al. J. Mater. Res. Technol., 8, 6115, (2019).
51. Devi, H.S.; Boda, M.A.; Shah, M.A.; Parveen, S.; Wani, A.H. Green Process. Synth., 8, 38, (2019).
52. Bhuiyan, S.H.; Miah, M.Y.; Paul, S.C.; Das Aka, T.; Saha, O.; Rahaman, M.; Sharif, J.I.; Habiba, O. Ashaduzzaman. Heliyon, 6, 04603, (2020).
53. Y. Wang, Z. Shang, T. Wu, J. Fan, X. Chen, J. Mol. Catal. A. Chem., 253, 212, (2006).
54. A. Rahmati, K. Vakili, Amino Acids, 39, 911, (2021).
55. J. Han, Y. Xu, Y. Su, X. She, X. Pan, Catal. Commun., 9, 2077, (2008).
56. P.R. Desai, N.J. Jain, R.K. Sharma, P. Bahadur, Colloids Surf A., 178, 57, (2001).
57. M.J. Rosen, X.Y. Hua, J Colloid Interface Sci., 86, 164, (1982).
58. Y.C. Luiking, G.A.M.T. Have, R.R. Wolfe, N.E.P. Deutz, Am J Physiol Endocrinol Metab. 303, 1177, (2012).
59. S. Kerkhofs, T. Willhammar, H.V.D. Noortgate, C.E.A. Kirschhock, E. Breynaert, G.V. Tendeloo, S. Bals, J.A. Martens, Chem Mater., 27, 5161, (2015).
60. R. Jenkins, R.L. Snyder, Introduction to X-ray Powder Diffractometry. (John Wiley & Sons, NY, 1996).
61. E. Shah, H.P. Soni , RSC Adv., 3, 17453, (2013).
62. E. Shah, P. Mahapatra , A.V. Bedekar , H.P. Soni , RSC Adv ., 5, 26291, (2015).

63. M. Kakihana, T. Nagumo , O. Makoto , H. Kakihana , J Phys Chem., 91, 6128, (1987).
64. T. K. Jain, M. A. Morales, S. K. Sahoo, D. L. Leslie-Pelecky, V. Labhasetwar, Mol. Pharm., 2, 194, (2005).
65. M. L. Neel, Ann. Phys., 12, 137, (1948).
66. J. H. Lee, Y.M. Huh, Y.W. Jun, J.W. Seo, J.T. Jang, H.T. Song, S. Kim, E.J. Cho, H.G. Yoon, J.S. Suh, J. Cheon, Nat Med., 13, 95, (2007).
67. R. A. McCurrie, Ferromagnetic Materials: Structure and Properties. (Academic Press, London, 1994).
68. J. T. Jang, H. Nah, J.H. Lee, S.H. Moon, M.G. Kim, J. Cheon, Angew Chem Int Ed., 48, 1234, (2009).
69. K.M. Krishnan, IEEE Trans Magn., 46, 2523, (2010).
70. U. Schwertmann, R.M. Cornel, (Wiley-VCH, Weinheim, 2000).
71. S. Xuan,Y.XJ. Wang, J.C. Yu, KC.F. Leung, Chem Mater., 21, 5079, (2009).
72. J. Liu, Y. Bin, M. Matsuo, J. Phys. Chem. C., 116, 134, (2012).
73. F. Grasset ,N. Labhsetwar ,D. Li, D.C. Park, N. Saito , H. Haneda , O. Cador , T. Roisnel ,S. Mornet, E. Duguet, J. Portier , J. Etourneau, Langmuir., 18, 8209, (2002).
74. S. Kamali-M, A.M. Blixt, L. Haggstrom, R. Wappling, V. Stanciu, P. Nordblad, J Magn Magn Mater., 272, 1263, (2004).